

Derivatives in Proton CT

Max Aehle^a Johan Alme^b Gergely Gábor Barnaföldi^c
Johannes Blühdorn^a Tea Bodova^b Vyacheslav Borshchov^d
Anthony van den Brink^e Mamdouh Chaar^b
Viljar Eikeland^b Gregory Feofilov^f Christoph Garth^g
Nicolas R. Gauger^a Georgi Genov^b Ola Grøttvik^b
Håvard Helstrup^h Sergey Igolkin^f Ralf Keidelⁱ
Chinorat Kobdaj^j Tobias Kortusⁱ Viktor Leonhardt^g
Shruti Mehendale^b Raju Ningappa Mulawadeⁱ
Odd Harald Odland^{k, b} George O'Neill^b Gábor Papp^l
Thomas Peitzmann^e Helge Egil Seime Pettersen^k
Pierluigi Piersimoni^{b, m} Rohit Pochampalli^a
Maksym Protsenko^d Max Rauch^b Attiq Ur Rehman^b
Matthias Richterⁿ Dieter Röhrich^b Max Sagebaum^a
Joshua Santanaⁱ Alexander Schillingⁱ Joao Seco^{o, p}
Arnon Songmoolnak^{b, j} Jarle Rambo Sølvi^q
Ganesh Tambave^b Ihor Tymchuk^d Kjetil Ullaland^b
Monika Varga-Kofarago^c Lennart Volz^{r, s} Boris Wagner^b
Steffen Wendzelⁱ Alexander Wiebelⁱ RenZheng Xiao^{b, t}
Shiming Yang^b Hiroki Yokoyama^e Sebastian Zillienⁱ

February 14, 2022

^aChair for Scientific Computing, TU Kaiserslautern, 67663 Kaiserslautern, Germany; ^bDepartment of Physics and Technology, University of Bergen, 5007 Bergen, Norway; ^cWigner Research Centre for Physics, Budapest, Hungary; ^dResearch and Production Enterprise “LTU” (RPE LTU), Kharkiv, Ukraine; ^eInstitute for Subatomic Physics, Utrecht University/Nikhef, Utrecht, Netherlands; ^fSt. Petersburg University, St. Petersburg, Russia; ^gScientific Visualization Lab, TU Kaiserslautern, 67663 Kaiserslautern, Germany; ^hDepartment of Computer Science, Electrical Engineering and Mathematical Sciences, Western Norway University of Applied Sciences, 5020 Bergen, Norway; ⁱCenter for Technology and Transfer (ZTT), University of Applied Sciences Worms, Worms, Germany; ^jInstitute of Science,

Suranaree University of Technology, Nakhon Ratchasima, Thailand; ^kDepartment of Oncology and Medical Physics, Haukeland University Hospital, 5021 Bergen, Norway; ^lInstitute for Physics, Eötvös Loránd University, 1/A Pázmány P. Sétány, H-1117 Budapest, Hungary; ^mUniCamillus – Saint Camillus International University of Health Sciences, Rome, Italy; ⁿDepartment of Physics, University of Oslo, 0371 Oslo, Norway; ^oDepartment of Biomedical Physics in Radiation Oncology, DKFZ—German Cancer Research Center, Heidelberg, Germany; ^pDepartment of Physics and Astronomy, Heidelberg University, Heidelberg, Germany; ^qDepartment of Diagnostic Physics, Division of Radiology and Nuclear Medicine, Oslo University Hospital, Oslo, Norway; ^rBiophysics, GSI Helmholtz Center for Heavy Ion Research GmbH, Darmstadt, Germany; ^sDepartment of Medical Physics and Biomedical Engineering, University College London, London, UK; ^tCollege of Mechanical & Power Engineering, China Three Gorges University, Yichang, People’s Republic of China

Algorithmic derivatives can be useful to quantify uncertainties and optimize parameters using computer simulations. Whether they actually are, depends on how “well-linearizable” the program is.

Proton computed tomography (pCT) is a medical imaging technology with the potential to increase the spatial accuracy of the dose delivered in proton-beam radiotherapy. The Bergen pCT collaboration is developing and constructing a digital tracking calorimeter (DTC) to measure the position, direction and energy of protons after they passed through a patient, and a software pipeline to process these data into a pCT image.

We revisit the software pipeline from the perspective of algorithmic differentiation (AD). In the early subprocedures, several obstacles such as discrete variables or frequent discontinuities were identified, and are probably tackled best by using surrogate models. The model-based iterative reconstruction (MBIR) subprocedure in the end seems to be AD-ready, and we propose changes in the AD workflow that can reduce the memory consumption in reverse mode.

1 Introduction

The option of cancer treatment using beams of charged particles, mainly protons, is becoming more and more available on a world-wide scale. Its main advantage over conventional X-ray radiotherapy lies in a possibly lower dose outside the tumor, because the energy deposition of protons is concentrated around the *Bragg peak* in a particular depth inside the patient. The current state-of-the-art method of obtaining the *relative stopping power* (RSP) map that is needed to calculate the water-equivalent depth, and therefore to plan the treatment, is to convert from the *Hounsfield units* (HU) of an X-ray (single-energy or dual-energy) CT acquisition; this approach comes with an uncertainty of the Bragg peak location of up to 3% of the range.^{1,2,3} Besides dual-energy X-ray CT, the direct measurement of a *proton CT* image using a higher-energy proton beam and a particle detector produces a direct RSP map and has the potential to be more accurate.^{4,5}

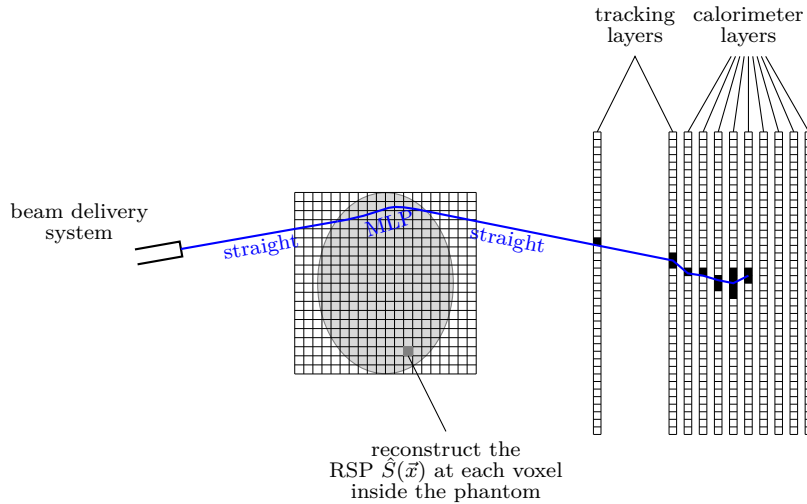


Figure 1: Schematic figure of the scanning process.

To this end, the Bergen pCT collaboration⁶ is designing and building a high-granularity digital tracking calorimeter (DTC) as a clinical prototype to add imaging capabilities to an existing treatment facility for proton therapy. Its sensitive hardware consists of two “tracking” and 41 “calorimeter” layers of 108 ALPIDE (ALICE pixel detector) chips each. After traversing the patient, energetic protons will activate several pixels in each layer until they are stopped, as shown in figure 1. In each read-out cycle, the layer-wise binary activation images from hundreds of protons are collected and used to reconstruct the protons’ paths and ranges through the detector and thus their residual direction and energy after leaving the phantom. Based on this data from various beam positions and directions, a *model-based iterative reconstruction* (MBIR) algorithm approximates the 3D RSP image. These two main subprocedures are displayed in figure 2, along with a *Monte Carlo simulation* subprocedure to generate the detector output instead of a real device for testing and optimization purposes.

Regarding several computer science aspects of the image reconstruction process, the Bergen pCT collaboration joins efforts with the SIVERT research training group. Part of our work is the quantification of uncertainties with the help of *algorithmic differentiation* (AD), a tool that is currently also adopted in the fundamental physics community for detector optimization.⁷

The remainder of this paper is structured as follows. In section 2, we summarize all the computational steps of the software pipeline in greater detail. Section 3 is a general introduction into the purpose and calculation of derivatives of computer programs, and in section 4 we analyze the specific challenges regarding the software pipeline at hand. A very first practical result is cited in section 5.

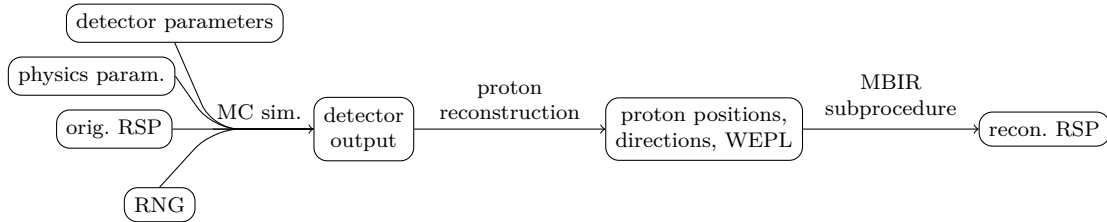


Figure 2: Overview of the pCT reconstruction pipeline.

2 A Software Pipeline for pCT Data Processing

2.1 Proton CT

When energetic protons pass through matter, they slow down in a stochastic way, mainly due to inelastic interactions with the bound electrons. The average rate $\frac{\partial E}{\partial s}$ of kinetic energy E lost per travelled length s is called *stopping power*. We denote it by $S(E, \vec{x})$, indicating its dependency on the current energy E of the proton and the local material present at location \vec{x} . Using the symbol $S_w(E)$ for the stopping power of water at the energy E , the *relative stopping power* (RSP) is defined as

$$\hat{S}(\vec{x}) = \frac{S(E, \vec{x})}{S_w(E)}. \quad (1)$$

The dependency on E has been dropped in the notation because in the relevant range between 30 MeV and 200 MeV, the RSP is essentially constant w. r. t. E .⁸ Proton therapy planning is based on CT images which show the spatial distribution of RSP across the scanned object, a simulated “phantom” in our study.

Let $\vec{x} : [0, \ell] \rightarrow \mathbb{R}^3$ be the arc-length parametrization of the path of a proton. Separating variables in the differential equation $\frac{\partial E(s)}{\partial s} = \hat{S}(\vec{x}(s)) \cdot S_w(E(s))$ and integrating, one obtains

$$\int_{E(0)}^{E(\ell)} \frac{1}{S_w(E)} dE = \int_0^\ell \hat{S}(\vec{x}(s)) ds. \quad (2)$$

This value is called the *water-equivalent path length*.

In list-mode pCT imaging, millions of protons are sent through the phantom, and their positions $\vec{x}(s)$, directions $\frac{d}{ds}\vec{x}(s)$ and energies $E(s)$ are recorded, both before entering ($s = 0$) and after leaving ($s = \ell$) the phantom. In the setup conceived by the Bergen pCT collaboration and sketched in figure 1, the exit measurements are performed by the digital tracking calorimeter (DTC), through the processing steps outlined in section 2.3. While many prototypes reported in the literature use an additional pair of front trackers,^{8,9,10,11,12,13} our setup infers the positions and directions of entering protons from the control of the beam delivery system, which is accurate enough.¹⁴

In general, *model-based iterative reconstruction* of the voxelized $\hat{S}(\vec{x})$ image means to

- form model equations, as follows: Given $E(0)$ and $E(\ell)$, the left hand side of (2) can be evaluated. Estimating the path $\vec{x}(s)$ from the positions and directions at

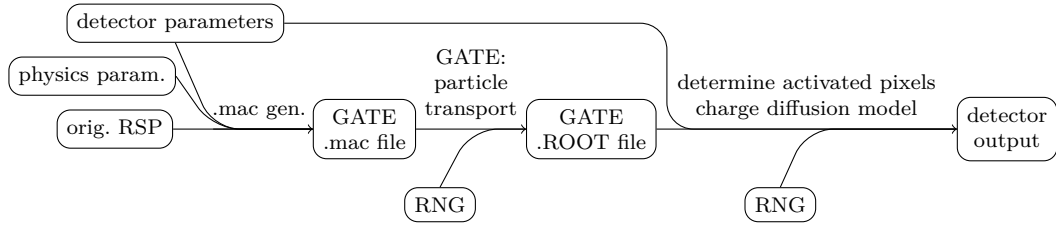


Figure 3: Computational steps of the Monte Carlo Simulation.

$s = 0, \ell$, the right hand side becomes a linear combination of the values of $\hat{S}(\vec{x})$ of the voxels intersecting the path. Thus (2) turns into one linear equation per proton.

- These model equations are then approximatively solved by an iterative numerical algorithm, that repeatedly improves a solution candidate to fit the model equations better and better.

We give more details on the MBIR subprocedure in section 2.4.

2.2 Monte Carlo Subprocedure

Figure 3 displays the intermediate variables and procedures of the Monte Carlo subprocedure to simulate the detector output. Its central step is the open-source software GATE¹⁵ for simulations in medical imaging and radiotherapy, based on the Geant4 toolkit for the simulation of the passage of particles through matter.^{16,17,18} Based on a description of the relevant physical properties of the complete detector-phantom setup, i. e.,

- the shape and material composition of the detector as well as the proton beam characteristics (*detector parameters*),
- the shape and material composition of the phantom (*original RSP*), and
- physics parameters like models and cross sections that define probability distributions for the relevant interactions between particles and matter, as well as output parameter setup (*physics parameters*),

GATE produces stochastically independent paths of single particles through the described setup. Whenever things happen with a certain probability distribution, the turnout for the proton at hand is decided by a random number from a pseudo random number generator (RNG).

The epitaxial layers of the ALPIDE chips are modelled as `crystalSD` volumes in GATE, so GATE records the positions and energy losses of all charged particles passing these volumes. In order to convert the data into a binary image of pixel activations, a spatial arrangement of the number of activated pixels that corresponds to the energy loss is randomly selected from a “library”.¹⁹ As approximately 100 protons pass through

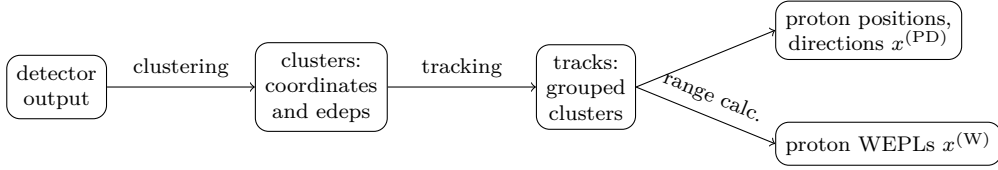


Figure 4: Computational steps of the proton reconstruction subprocedure.

the phantom during one read-out cycle of the real detector (depending on the detector parameters), a union of all activated pixels is formed to obtain the final binary image for each read-out cycle. The relationship between the pixel size and deposited energy for charged ions incident on the ALPIDE chip was determined experimentally.²⁰

2.3 Proton Reconstruction

Figure 4 displays the computational steps to convert the binary activation images per layer and read-out cycle, either produced by the real detector or by the Monte Carlo procedure in section 2.2, back to continuous coordinates and energies of protons.

Neighbouring (vertically and horizontally) activated pixels are grouped into *clusters* per layer and read-out cycle, because they likely were activated by the same proton. The proton’s coordinate is given by the cluster’s center of mass and its energy deposition is related to the size of the cluster.^{20,21}

In the *tracking* step, a track-following procedure²² attempts to match clusters in bordering layers likely belonging to the same particle trajectory. The angular change between the extrapolation of a growing track and cluster candidates in a given layer is minimized in a recursive fashion.^{19,23}

Based on the cluster positions in the two tracking layers of the DTC, the position and direction of the proton in the first tracking layer can be inferred. A vector $x^{(PD)}$ stores this data together with the position and direction of the beam source.

The proton’s residual WEPL before entering the detector can be estimated by a fit of the Bragg-Kleeman equation of Bortfeld^{24,25} to the energy depositions per layer.¹⁹ Its difference to the initial beam energy is stored in $x^{(W)}$. Failures of the tracking algorithms are usually due to pair-wise confusion between tracks from *multiple Coulomb scattering* (MCS), to the merging of close clusters, or to high-angle scattering. To this end, tracks with an unexpected distribution of energy depositions are attributed to secondary particles or mismatches in the tracking algorithm, and filtered out.²⁶

2.4 MBIR Subprocedure

As the name says, model-based iterative reconstruction algorithms repeatedly improve the RSP image to make it a better and better fit to the measurements of $x^{(PD)}$, $x^{(W)}$, according to the model equations (2).

While the paths of the protons in the air gaps between the beam delivery system, the phantom and the DTC can be assumed to be straight rays, inside the phantom they are

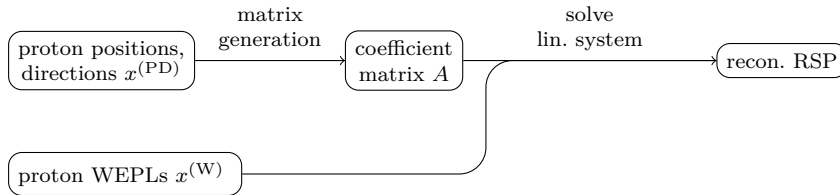


Figure 5: Computational steps of the MBIR subprocedure.

stochastic and unknown due to electromagnetic (MCS) and nuclear interactions with atomic nuclei. Using the model of MCS by Lynch and Dahl²⁷ and Gottschalk²⁸, and given the positions and directions $x^{(PD)}$ from section 2.3, the *most likely path* (MLP) can be analytically approximated in a maximum likelihood formalism.²⁹ The *extended MLP* formalism³⁰ also takes uncertainties of the positions and directions into account. Alternatively, a weighted cubic spline is a good approximation of the MLP.³¹ The WEPL of the proton is the integral of the RSP along the estimated path, and has also been reconstructed in section 2.3 as $x^{(W)}$. We therefore get a linear system of equations for the list y of all voxels of the RSP image,

$$A_{x^{(PD)}}y = x^{(W)}. \quad (3)$$

The entry (i, j) of the matrix $A = A_{x^{(PD)}}$ stores how much the RSP at voxel j influences the WEPL of proton i ; this value is related to the length of intersection of the proton’s path and the voxel’s volume, and thus depends on $x^{(PD)}$. As each proton passes through a minor fraction of all voxel volumes, A is typically sparse.

The matrix A is not a square matrix as the number of protons is independent of the dimensions of the RSP image. Therefore “solving (3)” is either meant in the least-squares sense, or additional objectives like noise reduction are taken into account via regularization or superiorization.³²

The two main computational steps of the MBIR subprocedure, generating the matrix $A_{x^{(PD)}}$ and solving the system (3), are displayed in figure 5. Several implementations of X-ray MBIR algorithms^{33,34} actually do not store the matrix in memory explicitly, because even in a sparse format it would be too large.³³ Rather, they implement *matrix-free solvers* like ART, SIRT, SART or DROP³⁵, which access the matrix only in specific ways, e. g. via (possibly transposed) matrix-vector products or calculating norms of all rows. The matrix elements can thus be regenerated on-the-fly to perform the specific operation demanded by the solver. In pCT, it is best to structure these operations as *policies* to be applied for each row of A : Due to the bent paths of protons, it is more efficient to make steps along a path and detect all the voxels it meets, rather than the other way round. Parallel architectures like GPUs can provide a significant speedup for operations whose policies can be executed concurrently for many rows.

3 Derivatives of Algorithms

Any computer program that computes a vector $y \in \mathbb{R}^m$ of *output variables* based on a vector $x \in \mathbb{R}^n$ of *input variables* defines a function $f : \mathbb{R}^n \rightarrow \mathbb{R}^m$, that maps x to y . The function f may or may not be differentiable at any x ; if it is, its *Jacobian matrix* $f'(x) \in \mathbb{R}^{m \times n}$ contains all the partial derivatives

$$\frac{\partial y_j}{\partial x_i} = \lim_{h \rightarrow 0} \frac{f_j(x + h \cdot e^{(i)}) - f_j(x)}{h} \quad (4)$$

where $e^{(i)}$ is the i -th unit vector.

Typically, f is differentiable for almost all x because the computer program is a big composition of elementary functions like $+$, \cdot , \sin , $\sqrt{\cdot}$, $|\cdot|$ etc. that are differentiable almost everywhere, due to the chain rule. Reasons for not differentiability of f at a particular x include the following cases:

- An elementary function is evaluated at an argument where it is not differentiable, like the abs function $|\cdot|$ at 0.
- An elementary function is evaluated at an argument where it is not even continuous, like rounding at $k + \frac{1}{2}$ for integers k .
- An elementary function is evaluated at an argument where it is not even defined, like division by zero.
- A control flow primitive like `if` or `while` makes a conditional jump depending on a $=$, \geq or \leq comparison of values that happen to be equal.

Although differentiability and derivatives are local concepts, they can be used for extrapolation by *Taylor's theorem*. A precise statement³⁶ in first order is that if f is twice continuously differentiable, for each \hat{x} there are constants C , D such that the error of the linearization

$$f(x) \approx f(\hat{x}) + f'(\hat{x}) \cdot (x - \hat{x}) \quad (5)$$

is bound by $C \cdot |x - \hat{x}|^2$ for all x with $|x - \hat{x}| < D$. The Taylor expansion (5) is frequently used as a heuristic or motivation even if the differentiability requirements are violated. This is only meaningful if the “amount” or “density” of the non-differentiable spots x listed above is low, and f' has no steep gradients. To assess the range in which the linearization (5) is valid, one can plot $f(x) - f(\hat{x})$ against $|x - \hat{x}|$ and compare to the graph of a proportionality relation. We call it the *linearizability range*.

The two applications discussed in the next sections 3.1 and 3.2 rely on (5). Ways to obtain derivatives are discussed in the subsequent sections 3.3 to 3.5.

3.1 Quantification of Uncertainty

If the value of an input x is approximated by \hat{x} and the resulting uncertainty of $f(x)$ is sought, $f'(\hat{x})$ contains the relevant information to measure the amplification of errors: According to the Taylor expansion (5), the deviation of x from \hat{x} gives rise to an approximate deviation of $f(x)$ from $f(\hat{x})$ by $f'(\hat{x}) \cdot (x - \hat{x})$.

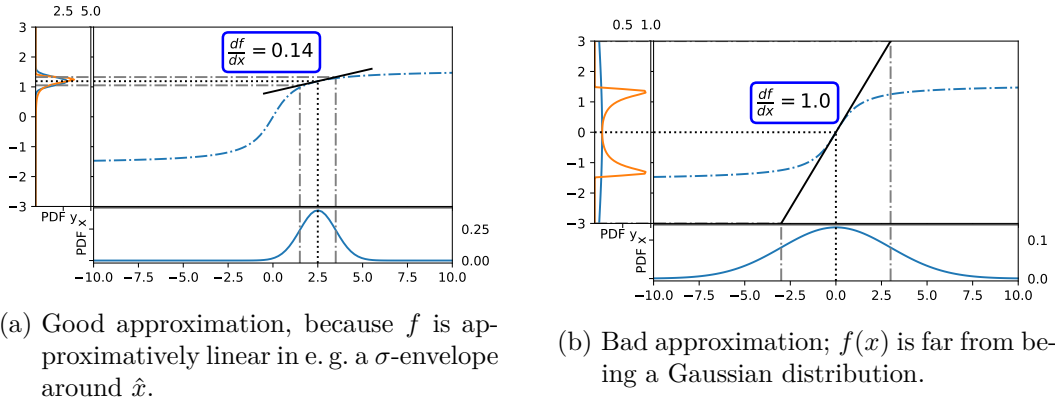


Figure 6: A function f , shown by the dash-dotted plot in the central box, is applied to a Gaussian random variable x whose probability density function (PDF) is shown in the bottom graph. In the left box we show the true distribution of $f(x)$ (in orange) and the normal distribution with variance according to (6) (in blue).

A more specific analysis is possible when we model the uncertainty in the input x using a Gaussian distribution with mean \hat{x} and covariance matrix Σ_x . Approximating f with its linearization (5), the output $f(x)$ is a Gaussian distribution with mean $f(\hat{x})$ and covariance matrix

$$\Sigma_{f(x)} = f'(\hat{x}) \cdot \Sigma_x \cdot f'(\hat{x})^T. \quad (6)$$

We are interested in uncertainties of the reconstructed RSP image as a result of the MBIR subprocedure, or the uncertainties of results of further image processing like contour lines³⁷. Possible input variables of known uncertainty are the detector output or reconstructed proton paths. All steps in the pipeline from this input to the output must be differentiated in order to apply (6). Thus derivatives of GATE are not required in any case.

Uncertainties in the input should be “unlikely” to go beyond the linearizability range. Otherwise, f is not approximated well by its linearization for a significant amount of possible inputs x and (6) cannot be used, as illustrated in figure 6.

No matter how non-smooth f is, Monte Carlo simulation can be used alternatively to propagate a random variable x through a computer program f and estimate the statistical properties of the random variable $f(x)$. The more samples are used, the better the Monte Carlo estimate becomes but the more run-time must be spent.

3.2 Gradient-Based Optimization

In the case that f has a single output variable ($m = 1$), optimization seeks to find a value for x that minimizes (or maximizes) this *objective function*. The Jacobian $f'(x) \in \mathbb{R}^{1 \times n}$ is a row vector whose transpose points into the *direction of steepest ascent* according to (5), i. e. shifting x in the opposite direction is a sensible attempt to make the value

of f smaller. This is the basic idea of gradient-based optimization algorithms. Neural-network training algorithms like *ADAM* also belong to this category, with the training error of the neural network as the objective function.

In order to perform an end-to-end optimization of the detector parameters to minimize an objective function based on the reconstructed RSP, all parts of the pipeline in figure 2 would have to be differentiated, including GATE.

Lack of differentiability and consequently, lack of explicit gradients precludes the guarantee that a gradient based optimization algorithm can converge to a local minimum. Instead of using the gradient to find a descent direction, one could alternatively iterate through all coordinate directions, use random choices or a surrogate model. Many *derivative-free optimization* algorithms have been proposed in the literature.³⁸ However, few of them are able to deal with 300 unknowns or more.³⁹

3.3 Numeric Differentiation

Numerical differentiation approximates the limit (4) through values of $f(x)$ at several close locations $x \approx \hat{x}$, like the forward and central difference quotients

$$\frac{f_j(\hat{x} + h \cdot e^{(i)}) - f_j(\hat{x})}{h} \quad \text{or} \quad \frac{f_j(\hat{x} + h \cdot e^{(i)}) - f_j(\hat{x} - h \cdot e^{(i)})}{2h} \quad (7)$$

as approximations for $\left. \frac{\partial y_j}{\partial x_i} \right|_{x=\hat{x}}$. The smaller $|h| \neq 0$ is chosen,

- the better the difference quotients (7) approximate the limit (4) from a purely mathematical perspective, but
- the worse are floating-point errors due to the subtraction of numbers of equal magnitude in the numerator.

The number of function evaluations is proportional to the number of input variables.

3.4 Analytic Differentiation

If a representation of $f(x)$ as a symbolic expression in x is known, the expression could be symbolically differentiated according to the rules of differential calculus, either on paper or by a computer algebra system. This may be feasible for small (steps of) algorithms with a clear mathematical structure, however at the cost that a lot of additional code must be produced and maintained.

3.5 Algorithmic Differentiation

Ideally, algorithmic differentiation^{40,41} (AD) combines the advantages of non-invasiveness and accuracy up to floating-point precision. Similar to analytic differentiation, AD depends on the code of f , in the sense that it assembles the derivative $f'(\hat{x})$ from the analytically known derivatives of the elementary operations that were used to compute $f(\hat{x})$. However, AD deals with numbers, not symbolic terms.

3.5.1 Forward Mode

The *forward mode* of AD can be used to compute one column of the Jacobian $f'(\hat{x})$, i. e. the partial derivatives $\left. \frac{\partial y_j}{\partial x_i} \right|_{x=\hat{x}}$ of all output variables y_j with respect to a single input variable $x_{\hat{i}}$, within a time and memory budget proportional to the budget needed to evaluate $f(\hat{x})$. It extends each intermediate variable a by its *tangent variable* \dot{a} storing the derivative of a with respect to $x_{\hat{i}}$. \dot{a} can be computed alongside a according to the rules of differentiation: e. g., for $a = b + c$ we have $\dot{a} = \dot{b} + \dot{c}$, for $a = b \cdot c$ we have $\dot{a} = b \cdot \dot{c} + \dot{b} \cdot c$, more generally for $a = \phi(b_1, \dots, b_k)$ we have

$$\dot{a} = \frac{\partial \phi}{\partial b_1} \cdot \dot{b}_1 + \dots + \frac{\partial \phi}{\partial b_k} \cdot \dot{b}_k. \quad (8)$$

The tangent variables of the input variables are initialized with

$$\dot{x}_i = \frac{\partial x_i}{\partial x_{\hat{i}}} = \begin{cases} 1, & i = \hat{i} \\ 0, & i \neq \hat{i}. \end{cases} \quad (9)$$

As differentiation is linear, the *Jacobi-vector product* $f'(\hat{x}) \cdot v$ with any $v \in \mathbb{R}^n$ can be computed by initializing with $\dot{x} = v$ instead.

3.5.2 Reverse Mode

The *reverse mode* of AD can be used to compute one row of the Jacobian $f'(\hat{x})$, i. e. the partial derivatives $\left. \frac{\partial y_j}{\partial x_i} \right|_{x=\hat{x}}$ of a single output variable y_j with respect to all input variables x_i , within a time budget proportional to the budget needed to evaluate $f(\hat{x})$. Therefore it is especially suited for optimization tasks where there is only one output variable. It extends each intermediate variable a by its *adjoint variable* \bar{a} storing the derivative of y_j with respect to a (as if it were an additional input variable). The adjoint variables are computed by going through the statements of f in reverse order, updating the adjoint variables in each step: A general statement $a = \phi(b_1, \dots, b_k)$ leads to the update

$$\bar{b}_1 += \frac{\partial \phi}{\partial b_1} \cdot \bar{a}, \quad \dots, \quad \bar{b}_k += \frac{\partial \phi}{\partial b_k} \cdot \bar{a}, \quad \bar{a} = 0. \quad (10)$$

As the partial derivatives $\frac{\partial \phi}{\partial b_1}, \dots, \frac{\partial \phi}{\partial b_k}$ usually depend on b_1, \dots, b_k , either of them must be recorded during the computation of $f(\hat{x})$ on a first-in-last-out data structure (stack) called the *tape*.

The adjoint variables of the output variables are initialized with

$$\bar{y}_j = \frac{\partial y_j}{\partial y_j} = \begin{cases} 1, & j = \hat{j} \\ 0, & j \neq \hat{j}. \end{cases} \quad (11)$$

As differentiation is linear, the *vector-Jacobi product* $w \cdot f'(\hat{x})$ with any $w \in \mathbb{R}^{1 \times m}$ can be computed by initializing with $\bar{y} = w$ instead.

3.5.3 Implementations

The augmentation of elementary operations in the original program f with AD arithmetics (8), (10) (and recording in reverse mode) can take place at different steps of the building process:

- explicitly in the source code by *source transformation* tools like TAPENADE⁴²,
- through language features like polymorphism and *operator overloading* for a new datatype replacing `double`, by tools like ADOL-C⁴³, CoDiPack⁴⁴ or autograd⁴⁵,
- by a modified or special compiler, e. g. CLAD⁴⁶, Enzyme⁴⁷.

For an overview of tools and applications, visit <https://www.autodiff.org>.

3.5.4 Adaptations to the Primal Program

AD tools like those listed in the previous section 3.5.3 can often be applied “blindly” to any computer program to obtain algorithmic derivatives in an “automatic” fashion. However, for complex simulations further program-specific adaptations might be necessary.

For example, techniques like *checkpointing*⁴⁸ or *reverse accumulation* can reduce the memory consumption of the tape in reverse mode but require manual modifications of the primal program.

Another reason for revisiting the primal code is given by the fact that it does only approximate the “*true*” function, through which we *actually* want to propagate uncertainties, or that we *actually* want to optimize. Good function approximation does not guarantee that the corresponding derivatives are also well-approximated.⁴⁹ To illustrate this, figure 7 shows a smooth function (black graph) and value-wisely good approximations (blue graphs). In (b), the derivative of the approximation is zero everywhere except where the approximation jumps. In (c), a low-magnitude but high-frequency component of the approximation adds high-magnitude noise to the derivative. In these cases, the exact derivative of the approximation is entirely unrelated to the derivative of the true function and thus cannot be of any use to the propagation of uncertainties through, or the optimization of, the true function. Adaptations of the computer program might be necessary to ensure that it also a good approximation derivative-wise, as in (a). An example for this is given in the next section 3.5.5.

3.5.5 Differentiating the “Solve” Operation

The last subprocedure of the reconstruction pipeline in figure 2 is to compute y from x by solving a (linear) system of equations $g(x, y) = 0$. Iterative algorithms repeatedly improve a candidate solution until it satisfies certain convergence criteria; thus they are inherently approximative. As detailed in the previous section 3.5.4, primal convergence does not imply convergence of the derivatives; see figure 8 for a related observation. We can however avoid issues like that by exploiting the mathematically simple structure of the problem solved by the iterative algorithm, as follows.

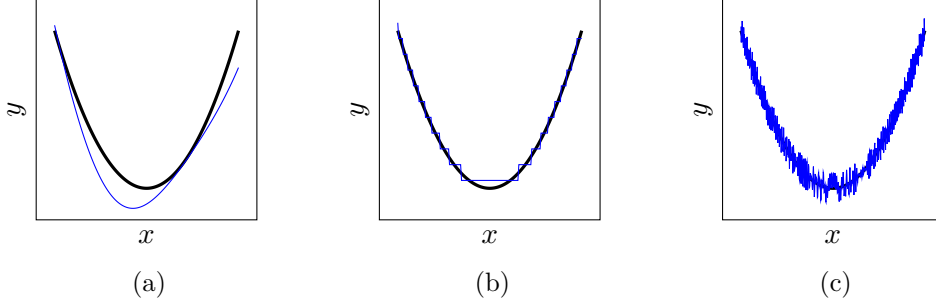


Figure 7: Good function approximations need not yield correspondingly good derivative approximations.

Given any set of equations $g(x, y) = 0$, the derivative of y with respect to x is analytically known as $-(\frac{\partial g}{\partial y})^{-1} \frac{\partial g}{\partial x}$ by the implicit function theorem. This allows to apply (8), (10) to the mathematical “solve” task as if it were a single statement of the code:

- In forward mode, (8) reads

$$\dot{y} = - \left(\frac{\partial g}{\partial y} \right)^{-1} \frac{\partial g}{\partial x} \cdot \dot{x}. \quad (12)$$

- In reverse mode, according to (10) we have to update

$$\bar{x} += -\bar{y} \cdot \left(\frac{\partial g}{\partial y} \right)^{-1} \frac{\partial g}{\partial x}, \quad \bar{y} = 0. \quad (13)$$

Instead of forming the inverse matrices in (12), (13), linear systems with the coefficient matrices $\frac{\partial g}{\partial y}$, $(\frac{\partial g}{\partial y})^T$ and column-vector right-hand sides $\frac{\partial g}{\partial x} \cdot \dot{x}$, \bar{y}^T must be solved, respectively. Ideally, this is done by a matrix-free solver that only accesses the matrix by multiplying it with vectors, as this operation can be performed by AD, just like the multiplication with $\frac{\partial g}{\partial x}$. To sum up, a forward-mode or reverse-mode differentiation of the loop in “solve $g(x, y) = 0$ ” can be replaced by a loop over forward-mode or reverse-mode differentiations of g , respectively.

4 Challenges for Differentiating the Pipeline

As detailed in section 3.5.4 based on figure 7, algorithms designed without an AD option in mind might need manual adaptations to make sure that their derivatives approximate the “true” function’s derivatives.

Besides, the linearization (5) is only helpful for the quantification of uncertainties and for optimization if the true function is “sufficiently smooth”, as discussed in sections 3.1 and 3.2.

In this section, we discuss these aspects for the software pipeline outlined in section 2.

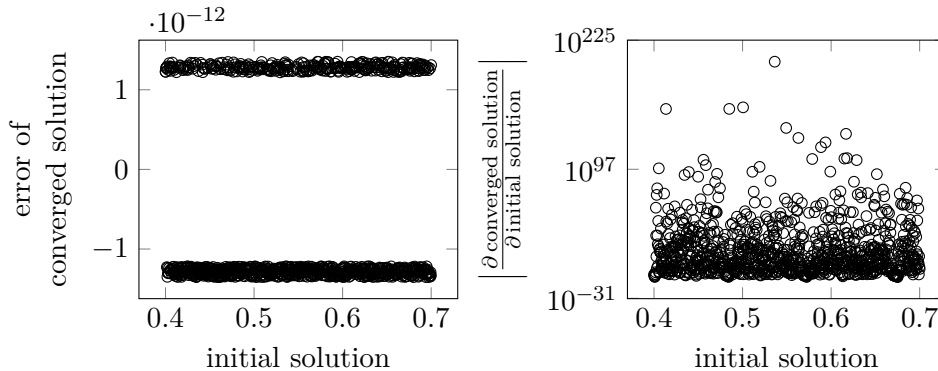


Figure 8: While the damped Newton scheme $x^{(k+1)} = x^{(k)} - \alpha g(x^{(k)})/g'(x^{(k)})$ converges to the single real solution of $g(x) = x^3 - 2x + 2$, the derivative of the converged solution with respect to the initial solution $x^{(0)}$ is far from 0. Here, $\alpha = 0.1$ and the solver was stopped as soon as $|g(x^{(k)})| < 10^{-11}$.

4.1 Discrete Variables Related to Detector Output

The detector output consists of pixel activations that are either 0 or 1, i. e. take a *discrete* value, as opposed to *continuous* coordinates, energies etc. The continuous output of GATE is mapped into discrete values by the charge diffusion model’s choice of which pixels to activate. The proton reconstruction subprocedure maps the discrete values back into a continuous range.

As the local behaviour of any function into a discrete set is either “constant” (not interesting) or “having a step” (not differentiable), we cannot make any use of derivative information here, as in figure 7b. Expressed differently, any discrete intermediate result comes from rounding of continuous coordinates, which erases all derivative information and is sometimes discontinuous.

One idea to fix this is to replace the continuous-to-discrete-to-continuous conversion by a surrogate model, which e. g. adds random errors to the output of GATE to model the charge diffusion model and proton reconstruction subprocedure.

4.2 Discrete Variables Related to Matrix Generation

While stepping along a path and determining the current voxel, an affine-linear function is applied to the current coordinates and the result is rounded; in the end, a certain path either intersects, or does not intersect, a certain voxel, which causes similar issues as the discrete variables of the previous section 4.1. If the precise intersection lengths were computed, the pipeline would be continuous, but non-differentiable w. r. t. $x^{(\text{PD})}$ whenever any path touches a voxel with intersection length zero. Using an *effective mean chord length*,⁵⁰ solely based on the tangent direction and averaging about the tangent shift, is likely to suffer from similar problems, as voxels still are either found to be hit or not.

To make the model smoother, we might think of “thick paths” or “fuzzy voxels”, where

also voxels without intersection with the path get a non-zero entry in the matrix A , that becomes smaller for more distant voxels.

4.3 Differentiation of Randomized Code

No meaningful information can be gained by differentiating GATE (and the charge diffusion model, if not bridged according to section 4.1) with respect to its “randomness input”, e. g. the seed of the RNG. Regarding the other partial derivatives (w. r. t. detector parameters etc.), the RNG seed is kept constant.

The usefulness of these derivatives eventually depends on how well-linearizable the pipeline is as a whole. As a first test, we however examined the range of input perturbations for which stand-alone GATE is linearizable according to (5):

In our setup, a single proton of initial energy x passes through a water phantom and several layers of the DTC. For various values of x that converge to $\hat{x} = 230$ MeV from the right, we extract four output variables from the ROOT file produced by GATE: The energy depositions $f_1(x)$, $f_2(x)$, and a position coordinate $f_3(x)$, $f_4(x)$, in the first and second tracking layer of the DTC, respectively. Figure 9 shows the deviation of these four output variables plotted against $(x - \hat{x})$.

For low perturbations $x - \hat{x}$ of the beam energy, the log-log plot shows a straight line with slope 1, indicating that the linearization (5) is a good approximation. However, after some threshold perturbation, the approximation error of the energy deposition rises suddenly. As apparent from figure 10, f is discontinuous for some $x \approx 230.01$ MeV, and there is around one discontinuity per 0.1 MeV.

One possible explanation for high density of discontinuities is that changes in the control flow severely affect the way how GATE interprets the randomness input: If for example, due to a small perturbation in an input, a `while` statement needs an additional loop and draws some additional numbers from the RNG, the subsequent code will see a shifted sequence of random numbers and therefore behave completely different. This situation is similar to potentially concurrent calls to a RNG in a multi-threaded environment. Using a series of independent RNG objects instead might remove discontinuities.

We should recall here that frequent discontinuities do not deteriorate the accuracy of AD for computing derivatives if they exist for the respective input. However, they diminish the accuracy of the linearization formula (5), and therefore the value of the derivatives for applications in sections 3.1 and 3.2 regarding stand-alone GATE.

Either way, detector optimization depends on derivatives of the pipeline as a whole. The results of the GATE simulations of many independent protons are combined, and in this process the chaotic behavior might average out. We plan to perform a similar check on the complete pipeline to check this hypothesis.

In reverse mode, the black-box recording of each Monte Carlo iteration on the tape would have a large memory footprint. This can be avoided by only storing a *checkpoint* of the input data for each iteration, and recording the corresponding section of the tape right before it is needed for evaluation of the adjoint variables.⁵¹

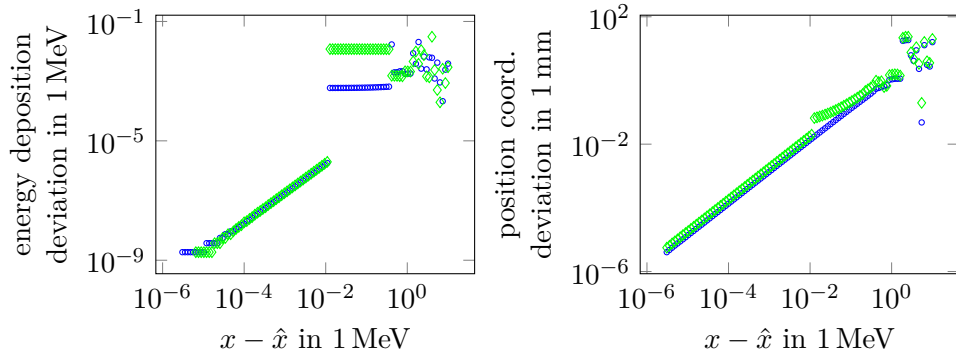


Figure 9: Numerical check whether GATE is well-linearizable: Against the input perturbation of the beam energy on the abscissa, this figure shows the resulting deviation $|f_j(x) - f_j(\hat{x})|$ of the energy deposition (left, $j = 1, 2$) and a position coordinate (right, $j = 3, 4$) in the first (blue, $j = 1, 3$) and second (green, $j = 2, 4$) tracking layer on the ordinate.

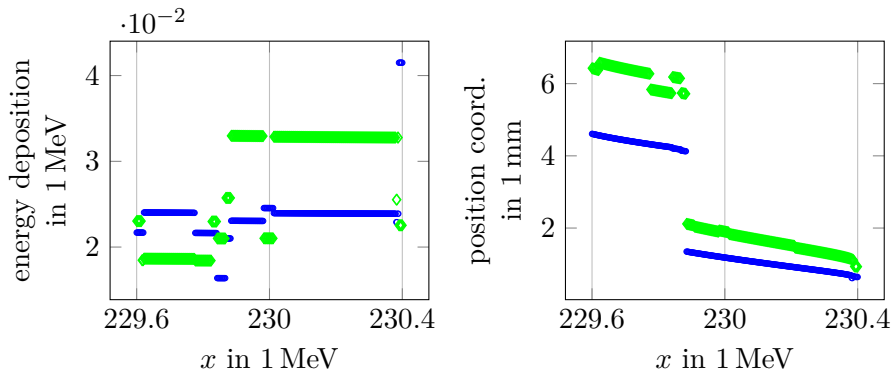


Figure 10: This is figure 9 with a different range and scale of the abscissa. f_1, f_2 have around one discontinuity per 0.1 MeV.

4.4 Differentiating the “Solve” Operation

In order to phrase (3) in the notation of section 3.5.5, we define $x = (x^{(W)}, x^{(PD)})$ and

$$g(x, y) = A_{x^{(PD)}}^T \left(A_{x^{(PD)}} \cdot y - x^{(W)} \right), \quad (14)$$

which is the residual of the *normal equation* to solve (3) in a least-squares sense. If a regularization term was included, its derivative would need to be added here as well.

The multiplication with $\frac{\partial g}{\partial y}$, $(\frac{\partial g}{\partial y})^T$, required by the matrix-free solver to evaluate the AD augmentations (12), (13), can actually be performed without AD: We know the analytical derivative

$$\frac{\partial g}{\partial y} = A_{x^{(PD)}}^T A_{x^{(PD)}} \quad (15)$$

and therefore can reuse the parallel implementation of the matrix-vector multiplication with A . If a regularization term was included, evaluating its second-order derivative with AD should not demand too much time and memory.

For the multiplication with $\frac{\partial g}{\partial x}$, we generally need to apply AD to an evaluation of g . The amount of memory required for the tape in reverse mode can be reduced by decomposing (14) as

$$g(x, y) = \sum_i \left(A_{x^{(PD)},i} \right)^T \cdot \left(A_{x^{(PD)},i} \cdot y - x_i^{(W)} \right), \quad (16)$$

where $A_{x^{(PD)},i}$ denotes the i -th row of $A_{x^{(PD)}}$, and differentiating each summand individually.

4.5 Differentiating Parallel Code

In principle, applying the forward mode of AD to parallel code is straightforward as elementary operations are simply augmented by computations of the tangent variables.

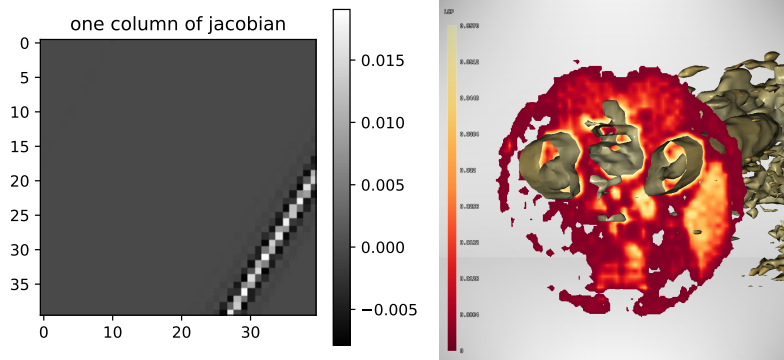
For black-box differentiation in the reverse mode, memory bandwidth puts an upper limit onto the achievable speed-up because all statements are recorded on the tape. Furthermore when evaluating the tape, performant parallel reads translate to non-performant parallel updates.

As discussed in section 4.4, most of the time during the MBIR subprocedure the taping can be turned off because we have a representation (15) without AD. AD is required to form the product with $\frac{\partial g}{\partial x}$, $(\frac{\partial g}{\partial x})^T$, but the decomposition (16) allows to differentiate many summands individually, which might allow a parallel execution again.

5 First Results

5.1 Derivatives of the Filtered Back-Projection Algorithm

As opposed to MBIR reconstruction algorithms that solve $Ay = x$ iteratively, backprojection-type algorithms reconstruct the tomographic image y from the line integrals x by a fixed



(a) Derivative of the reconstructed image w.r.t. a particular sinogram pixel. (b) Uncertainties of a contour surface visualized by the *level-crossing probability*⁵³ (LCP) colouring.

Figure 11: Using the derivative of the FBP algorithm.

set of linear operations that usually involve the multiplication with A^T . As they quickly compute a good approximation, they have been standard in commercial *X-ray* CT devices. We implemented the *Filtered Back-Projection* (FBP) using AD, both in Python using TensorFlow⁵² and in C++ using CoDiPack⁴⁴, with matching results.³⁷ Figure 11a shows one column of its Jacobian matrix, i. e. the change of the reconstructed image if one sensor pixel changes. We used the Jacobian matrix according to (6) to propagate uncertainties in the sinogram x through the FBP algorithm to the reconstructed image y , and visualized it in figure 11b with the *level-crossing probability* colouring that indicates the likelihood of each voxel to be on the wrong side of the isocontour.⁵³ Note that all these results can be produced without AD because the FBP is a linear map.

6 Summary

We presented the algorithmic substeps of the Bergen pCT collaboration’s incipient software pipeline, with special focus on linearizability. From back to front:

- The situation is good regarding the *MBIR subprocedure*, in which the RSP image is computed from the reconstructed position, direction and energy data of the protons as the least-squares solution of a linear system. The derivative of this step can likely be obtained by automatic differentiation when the mathematical structure of the problem is exploited. If the non-differentiable rounding operations during matrix generation turn out to be problematic, one should try out “thick paths”.
- The *proton reconstruction* subprocedure involves many discrete variables, which behave as constants in any differentiable chain of functions. This includes the layer-wise binary activation images of each read-out cycle as the subprocedure’s input.

Any uncertainty quantification calculation based on derivatives must therefore use a “differentiable bridge” modelling the real proton reconstruction algorithms.

- Numerical experiments with GATE have shown that the *Monte-Carlo simulation* subprocedure likely is numerically differentiable, however its linearization is accurate in small ranges only. As the simulated physics are not chaotic, this could be implementation-specific. Either way, an optimization task would require a derivative of the whole pipeline rather than only GATE, so some of the “numerical chaos” might be averaged out.

7 Acknowledgements

We gratefully acknowledge the funding of the research training group SIVERT by the German federal state of Rhineland-Palatinate.

This work is supported by the Research Council of Norway (Norges forskningsråd) and the University of Bergen, grant number 250858; the Trond Mohn Foundation, grant number BFS2017TMT07; as well as the Hungarian NKFIH OTKA K135515 grant and the Wigner Scientific Computing Laboratory (WSCLAB).

References

- [1] Ming Yang et al. “Comprehensive analysis of proton range uncertainties related to patient stopping-power-ratio estimation using the stoichiometric calibration”. In: *Physics in Medicine and Biology* 57.13 (June 2012), pp. 4095–4115. DOI: 10.1088/0031-9155/57/13/4095. URL: <https://doi.org/10.1088/0031-9155/57/13/4095>.
- [2] Harald Paganetti. “Range uncertainties in proton therapy and the role of Monte Carlo simulations”. In: *Physics in Medicine and Biology* 57.11 (May 2012), R99–R117. DOI: 10.1088/0031-9155/57/11/r99. URL: <https://doi.org/10.1088/0031-9155/57/11/r99>.
- [3] Patrick Wohlfahrt and Christian Richter. “Status and innovations in pre-treatment CT imaging for proton therapy”. In: *The British Journal of Radiology* 93.1107 (Mar. 2020). 00004, p. 20190590. ISSN: 0007-1285, 1748-880X. DOI: 10.1259/bjr.20190590.
- [4] George Dedes et al. “Experimental comparison of proton CT and dual energy x-ray CT for relative stopping power estimation in proton therapy”. In: *Physics in Medicine & Biology* 64.16 (Aug. 14, 2019), p. 165002. ISSN: 1361-6560. DOI: 10.1088/1361-6560/ab2b72. URL: <https://iopscience.iop.org/article/10.1088/1361-6560/ab2b72> (visited on 12/11/2021).

- [5] M Yang et al. “Theoretical variance analysis of single- and dual-energy computed tomography methods for calculating proton stopping power ratios of biological tissues”. In: *Physics in Medicine and Biology* 55.5 (Mar. 7, 2010), pp. 1343–1362. ISSN: 0031-9155, 1361-6560. DOI: 10.1088/0031-9155/55/5/006. URL: <https://iopscience.iop.org/article/10.1088/0031-9155/55/5/006> (visited on 12/11/2021).
- [6] Johan Alme et al. “A High-Granularity Digital Tracking Calorimeter Optimized for Proton CT”. In: *Frontiers in Physics* 8 (2020), p. 460. ISSN: 2296-424X. DOI: 10.3389/fphy.2020.568243. URL: <https://www.frontiersin.org/article/10.3389/fphy.2020.568243>.
- [7] Atılım Güneş Baydin et al. “Toward Machine Learning Optimization of Experimental Design”. In: *Nuclear Physics News* 31.1 (Jan. 2, 2021), pp. 25–28. ISSN: 1061-9127, 1931-7336. DOI: 10.1080/10619127.2021.1881364. URL: <https://www.tandfonline.com/doi/full/10.1080/10619127.2021.1881364> (visited on 12/11/2021).
- [8] R. F. Hurley et al. “Water-equivalent path length calibration of a prototype proton CT scanner: Water-equivalent path length calibration for proton CT”. In: *Medical Physics* 39.5 (Apr. 13, 2012), pp. 2438–2446. ISSN: 00942405. DOI: 10.1118/1.3700173. URL: <http://doi.wiley.com/10.1118/1.3700173> (visited on 01/24/2022).
- [9] Sebastian Meyer et al. “Optimization and performance study of a proton CT system for pre-clinical small animal imaging”. In: *Physics in Medicine & Biology* 65.15 (Aug. 13, 2020), p. 155008. ISSN: 1361-6560. DOI: 10.1088/1361-6560/ab8afc. URL: <https://iopscience.iop.org/article/10.1088/1361-6560/ab8afc> (visited on 01/21/2022).
- [10] Michela Esposito et al. “PRaVDA: The first solid-state system for proton computed tomography”. In: *Physica Medica* 55 (Nov. 2018), pp. 149–154. ISSN: 11201797. DOI: 10.1016/j.ejmp.2018.10.020. URL: <https://linkinghub.elsevier.com/retrieve/pii/S1120179718313073> (visited on 01/25/2022).
- [11] M. Scaringella et al. “The PRIMA (PRoton IMAGING) collaboration: Development of a proton Computed Tomography apparatus”. In: *Nuclear Instruments and Methods in Physics Research Section A: Accelerators, Spectrometers, Detectors and Associated Equipment* 730 (Dec. 2013), pp. 178–183. ISSN: 01689002. DOI: 10.1016/j.nima.2013.05.181. URL: <https://linkinghub.elsevier.com/retrieve/pii/S0168900213008036> (visited on 01/25/2022).
- [12] Y. Saraya et al. “Study of spatial resolution of proton computed tomography using a silicon strip detector”. In: *Nuclear Instruments and Methods in Physics Research Section A: Accelerators, Spectrometers, Detectors and Associated Equipment* 735 (Jan. 2014), pp. 485–489. ISSN: 01689002. DOI: 10.1016/j.nima.2013.09.051. URL: <https://linkinghub.elsevier.com/retrieve/pii/S0168900213012850> (visited on 01/25/2022).

- [13] Md. Naimuddin et al. “Development of a proton Computed Tomography detector system”. In: *Journal of Instrumentation* 11.2 (Feb. 4, 2016), pp. C02012–C02012. ISSN: 1748-0221. DOI: 10.1088/1748-0221/11/02/C02012. URL: <https://iopscience.iop.org/article/10.1088/1748-0221/11/02/C02012> (visited on 01/25/2022).
- [14] Jarle Rambo Sølve et al. “Image quality of list-mode proton imaging without front trackers”. In: *Physics in Medicine & Biology* 65.13 (July 2020). 00000, p. 135012. ISSN: 1361-6560. DOI: 10.1088/1361-6560/ab8ddb.
- [15] S. Jan et al. “GATE - Geant4 Application for Tomographic Emission: a simulation toolkit for PET and SPECT”. In: *Physics in Medicine and Biology* 49.19 (Oct. 2004), pp. 4543–4561. ISSN: 0031-9155. URL: <https://www.ncbi.nlm.nih.gov/pmc/articles/PMC3267383/> (visited on 10/19/2020).
- [16] S. Agostinelli et al. “Geant4—a simulation toolkit”. en. In: *Nuclear Instruments and Methods in Physics Research Section A: Accelerators, Spectrometers, Detectors and Associated Equipment* 506.3 (July 2003), pp. 250–303. ISSN: 0168-9002. DOI: 10.1016/S0168-9002(03)01368-8. URL: <http://www.sciencedirect.com/science/article/pii/S0168900203013688> (visited on 11/01/2020).
- [17] J. Allison et al. “Geant4 developments and applications”. In: *IEEE Transactions on Nuclear Science* 53.1 (Feb. 2006), pp. 270–278. ISSN: 0018-9499. DOI: 10.1109/TNS.2006.869826. URL: <http://ieeexplore.ieee.org/document/1610988/> (visited on 12/08/2021).
- [18] J. Allison et al. “Recent developments in Geant4”. en. In: *Nuclear Instruments and Methods in Physics Research Section A: Accelerators, Spectrometers, Detectors and Associated Equipment* 835 (Nov. 2016), pp. 186–225. ISSN: 01689002. DOI: 10.1016/j.nima.2016.06.125. URL: <https://linkinghub.elsevier.com/retrieve/pii/S0168900216306957> (visited on 12/08/2021).
- [19] Helge Egil Seime Pettersen et al. “Design optimization of a pixel-based range telescope for proton computed tomography”. en. In: *Physica Medica* 63 (July 2019), pp. 87–97. ISSN: 11201797. DOI: 10.1016/j.ejmp.2019.05.026. URL: <https://linkinghub.elsevier.com/retrieve/pii/S1120179719301358> (visited on 12/08/2021).
- [20] Ganesh Tambave et al. “Characterization of monolithic CMOS pixel sensor chip with ion beams for application in particle computed tomography”. In: *Nuclear Instruments and Methods in Physics Research Section A: Accelerators, Spectrometers, Detectors and Associated Equipment* 958. Proceedings of the Vienna Conference of Instrumentation 2019 (Apr. 2020), p. 162626. ISSN: 01689002. DOI: 10.1016/j.nima.2019.162626.
- [21] Helge Egil Seime Pettersen et al. “Proton tracking in a high-granularity Digital Tracking Calorimeter for proton CT purposes”. In: *Nuclear Instruments and Methods in Physics Research Section A: Accelerators, Spectrometers, Detectors and Associated Equipment* 860 (July 2017), pp. 51–61. ISSN: 01689002. DOI: 10.1016/j.

- nima.2017.02.007. URL: <https://linkinghub.elsevier.com/retrieve/pii/S0168900217301882> (visited on 05/21/2019).
- [22] Are Strandlie and Rudolf Frühwirth. “Track and vertex reconstruction: From classical to adaptive methods”. In: *Reviews of Modern Physics* 82.2 (May 7, 2010), pp. 1419–1458. ISSN: 0034-6861, 1539-0756. DOI: 10.1103/RevModPhys.82.1419. URL: <https://link.aps.org/doi/10.1103/RevModPhys.82.1419> (visited on 07/03/2020).
- [23] Helge Egil Seime Pettersen et al. “Proton Tracking Algorithm in a Pixel-Based Range Telescope for Proton Computed Tomography”. In: *arXiv:2006.09751 [physics]* (June 17, 2020). arXiv: 2006.09751. URL: <http://arxiv.org/abs/2006.09751> (visited on 12/03/2020).
- [24] Thomas Bortfeld. “An analytical approximation of the Bragg curve for therapeutic proton beams”. In: *Medical Physics* 24.12 (Dec. 1997), pp. 2024–2033. ISSN: 00942405. DOI: 10.1118/1.598116. URL: <http://doi.wiley.com/10.1118/1.598116> (visited on 12/10/2021).
- [25] Helge Egil Seime Pettersen et al. “Accuracy of parameterized proton range models; a comparison”. In: *Radiation Physics and Chemistry* 144 (Mar. 2018). IF 1.984, pp. 295–297. DOI: 10.1016/j.radphyschem.2017.08.028.
- [26] Helge Egil Seime Pettersen et al. “Investigating particle track topology for range telescopes in particle radiography using convolutional neural networks”. In: *Acta Oncologica* 60.11 (July 2021), pp. 1413–1418. ISSN: 0284-186X, 1651-226X. DOI: 10.1080/0284186X.2021.1949037.
- [27] Gerald R. Lynch and Orin I. Dahl. “Approximations to multiple Coulomb scattering”. In: *Nuclear Instruments and Methods in Physics Research Section B: Beam Interactions with Materials and Atoms* 58.1 (May 1991), pp. 6–10. ISSN: 0168583X. DOI: 10.1016/0168-583X(91)95671-Y. URL: <https://linkinghub.elsevier.com/retrieve/pii/0168583X9195671Y> (visited on 12/09/2021).
- [28] B. Gottschalk et al. “Multiple Coulomb scattering of 160 MeV protons”. In: *Nuclear Instruments and Methods in Physics Research Section B: Beam Interactions with Materials and Atoms* 74.4 (June 1993), pp. 467–490. ISSN: 0168583X. DOI: 10.1016/0168-583X(93)95944-Z. URL: <https://linkinghub.elsevier.com/retrieve/pii/0168583X9395944Z> (visited on 12/09/2021).
- [29] R. W. Schulte, S. N. Penfold, J. T. Tafas, and K. E. Schubert. “A maximum likelihood proton path formalism for application in proton computed tomography: Maximum likelihood path formalism for proton CT”. In: *Medical Physics* 35.11 (Oct. 13, 2008), pp. 4849–4856. ISSN: 00942405. DOI: 10.1118/1.2986139. URL: <http://doi.wiley.com/10.1118/1.2986139> (visited on 12/09/2021).

- [30] N Krah et al. “A comprehensive theoretical comparison of proton imaging set-ups in terms of spatial resolution”. In: *Physics in Medicine & Biology* 63.13 (July 2, 2018), p. 135013. ISSN: 1361-6560. DOI: 10.1088/1361-6560/aaca1f. URL: <https://iopscience.iop.org/article/10.1088/1361-6560/aaca1f> (visited on 12/09/2021).
- [31] Charles-Antoine Collins-Fekete et al. “A theoretical framework to predict the most likely ion path in particle imaging”. In: *Physics in Medicine & Biology* 62.5 (Mar. 2017), pp. 1777–1790. ISSN: 0031-9155, 1361-6560. DOI: 10.1088/1361-6560/aa58ce.
- [32] S. N. Penfold, R. W. Schulte, Y. Censor, and A. B. Rosenfeld. “Total variation superiorization schemes in proton computed tomography image reconstruction: Total variation superiorization in proton CT”. In: *Medical Physics* 37.11 (Oct. 20, 2010), pp. 5887–5895. ISSN: 00942405. DOI: 10.1118/1.3504603. URL: <http://doi.wiley.com/10.1118/1.3504603> (visited on 12/15/2021).
- [33] Ander Biguri, Manjit Dosanjh, Steven Hancock, and Manuchehr Soleimani. “TI-GRE: a MATLAB-GPU toolbox for CBCT image reconstruction”. In: *Biomedical Physics & Engineering Express* 2.5 (Sept. 8, 2016), p. 055010. ISSN: 2057-1976. DOI: 10.1088/2057-1976/2/5/055010. URL: <https://iopscience.iop.org/article/10.1088/2057-1976/2/5/055010> (visited on 12/15/2021).
- [34] Wim van Aarle et al. “The ASTRA Toolbox: A platform for advanced algorithm development in electron tomography”. In: *Ultramicroscopy* 157 (Oct. 2015), pp. 35–47. ISSN: 03043991. DOI: 10.1016/j.ultramic.2015.05.002. URL: <https://linkinghub.elsevier.com/retrieve/pii/S0304399115001060> (visited on 12/15/2021).
- [35] Scott Penfold and Yair Censor. “Techniques in Iterative Proton CT Image Reconstruction”. In: *Sensing and Imaging* 16.1 (Dec. 2015), p. 19. ISSN: 1557-2064, 1557-2072. DOI: 10.1007/s11220-015-0122-3. URL: <http://link.springer.com/10.1007/s11220-015-0122-3> (visited on 12/15/2021).
- [36] Robert M. Anderson. “Econ 204: Taylor’s Theorem”. Lecture Notes. Lecture Notes. University of California, Berkeley. URL: <https://eml.berkeley.edu/~anderson/Econ204/TaylorTheoremTimeless.pdf> (visited on 12/15/2021).
- [37] Max Ahle and Viktor Leonhardt. “Quantification and Visualization of Uncertainties in CT Reconstruction”. 7th Annual Loma Linda Workshop. Aug. 3, 2021. URL: <http://www.ionimaging.org/llu2021-overview/> (visited on 12/10/2021).
- [38] Jeffrey Larson, Matt Menickelly, and Stefan M. Wild. “Derivative-free optimization methods”. In: *Acta Numerica* 28 (May 1, 2019), pp. 287–404. ISSN: 0962-4929, 1474-0508. DOI: 10.1017/S0962492919000060. arXiv: 1904.11585. URL: <http://arxiv.org/abs/1904.11585> (visited on 12/10/2021).

- [39] Luis Miguel Rios and Nikolaos V. Sahinidis. “Derivative-free optimization: a review of algorithms and comparison of software implementations”. In: *Journal of Global Optimization* 56.3 (July 2013), pp. 1247–1293. ISSN: 0925-5001, 1573-2916. DOI: 10.1007/s10898-012-9951-y. URL: <https://link.springer.com/10.1007/s10898-012-9951-y> (visited on 12/10/2021).
- [40] Andreas Griewank and Andrea Walther. *Evaluating Derivatives*. Other Titles in Applied Mathematics. Society for Industrial and Applied Mathematics, Jan. 1, 2008. 448 pp. ISBN: 9780898716597. DOI: 10.1137/1.9780898717761. URL: <https://epubs.siam.org/doi/book/10.1137/1.9780898717761> (visited on 01/06/2022).
- [41] Uwe Naumann. *The Art of Differentiating Computer Programs: An Introduction to Algorithmic Differentiation*. Society for Industrial and Applied Mathematics, Jan. 2011. ISBN: 9781611972078. DOI: 10.1137/1.9781611972078. URL: <http://epubs.siam.org/doi/book/10.1137/1.9781611972078> (visited on 01/06/2022).
- [42] Laurent Hascoet and Valérie Pascual. “The Tapenade automatic differentiation tool: Principles, model, and specification”. In: *ACM Transactions on Mathematical Software* 39.3 (Apr. 2013), pp. 1–43. ISSN: 0098-3500, 1557-7295. DOI: 10.1145/2450153.2450158. URL: <https://dl.acm.org/doi/10.1145/2450153.2450158> (visited on 12/12/2021).
- [43] A. Walther and A. Griewank. “Getting started with ADOL-C”. In: *Combinatorial Scientific Computing*. Ed. by U. Naumann and O. Schenk. Chapman-Hall CRC Computational Science, 2012. Chap. 7, pp. 181–202.
- [44] M. Sagebaum, T. Albring, and N.R. Gauger. “High-Performance Derivative Computations using CoDiPack”. In: *ACM Transactions on Mathematical Software (TOMS)* 45.4 (Dec. 1, 2019). URL: <https://dl.acm.org/doi/abs/10.1145/3356900>. published.
- [45] Dougal Maclaurin, David Duvenaud, and Ryan P Adams. “Autograd: Effortless gradients in numpy”. In: *ICML 2015 AutoML Workshop*. Vol. 238. 2015, p. 5.
- [46] V. Vassilev et al. “Clad – Automatic Differentiation Using Clang and LLVM”. In: vol. 608. 1. IOP Publishing, May 2015, p. 012055. DOI: 10.1088/1742-6596/608/1/012055. URL: <https://iopscience.iop.org/article/10.1088/1742-6596/608/1/012055/pdf>.
- [47] William Moses and Valentin Churavy. “Instead of Rewriting Foreign Code for Machine Learning, Automatically Synthesize Fast Gradients”. In: *Advances in Neural Information Processing Systems*. Ed. by H. Larochelle et al. Vol. 33. Curran Associates, Inc., 2020, pp. 12472–12485. URL: <https://proceedings.neurips.cc/paper/2020/file/9332c513ef44b682e9347822c2e457ac-Paper.pdf>.
- [48] Benjamin Dauvergne and Laurent Hascoët. “The Data-Flow Equations of Checkpointing in Reverse Automatic Differentiation”. In: *Computational Science – ICCS 2006*. Ed. by Vassil N. Alexandrov, Geert Dick van Albada, Peter M. A. Sloot, and Jack Dongarra. Red. by David Hutchison et al. Vol. 3994. Berlin, Heidelberg:

- Springer Berlin Heidelberg, 2006, pp. 566–573. DOI: 10.1007/11758549_78. URL: http://link.springer.com/10.1007/11758549_78 (visited on 01/26/2022).
- [49] Ziv Sirkes and Eli Tziperman. “Finite Difference of Adjoint or Adjoint of Finite Difference?” In: *Monthly Weather Review* 125.12 (Dec. 1997), pp. 3373–3378. ISSN: 0027-0644, 1520-0493. DOI: 10.1175/1520-0493(1997)125<3373:FD0A0A>2.0.CO;2. URL: [http://journals.ametsoc.org/doi/10.1175/1520-0493\(1997\)125%3C3373:FD0A0A%3E2.0.CO;2](http://journals.ametsoc.org/doi/10.1175/1520-0493(1997)125%3C3373:FD0A0A%3E2.0.CO;2) (visited on 01/25/2022).
- [50] S. N. Penfold, A. B. Rosenfeld, R. W. Schulte, and K. E. Schubert. “A more accurate reconstruction system matrix for quantitative proton computed tomography: Reconstruction system matrix for quantitative proton CT”. In: *Medical Physics* 36.10 (Sept. 9, 2009), pp. 4511–4518. ISSN: 00942405. DOI: 10.1118/1.3218759. URL: <http://doi.wiley.com/10.1118/1.3218759> (visited on 12/15/2021).
- [51] Uwe Naumann and Jack Toit. *Adjoint Algorithmic Differentiation Tool Support for Typical Numerical Patterns in Computational Finance*. SSRN Scholarly Paper ID 3122293. Rochester, NY: Social Science Research Network, Feb. 12, 2018. URL: <https://papers.ssrn.com/abstract=3122293> (visited on 12/13/2021).
- [52] Martín Abadi et al. *TensorFlow: Large-Scale Machine Learning on Heterogeneous Systems*. Software available from tensorflow.org. 2015. URL: <https://www.tensorflow.org/>.
- [53] Kai Pöthkow and Hans-Christian Hege. “Positional Uncertainty of Isocontours: Condition Analysis and Probabilistic Measures”. In: *IEEE Transactions on Visualization and Computer Graphics* 17.10 (Oct. 2011), pp. 1393–1406. ISSN: 1077-2626. DOI: 10.1109/TVCG.2010.247. URL: <http://ieeexplore.ieee.org/document/5620906/> (visited on 12/10/2021).